MODELLING FLUID RESONANCE IN CONDUIT-CRACK COUPLED SYSTEMS: AN APPLICATION TO ENGLACIAL GEOMETRIES

by

MARIA MCQUILLAN

A THESIS

Presented to the Department of Earth Sciences
and the Graduate School of the University of Oregon
in partial fulfillment of the requirements
for the degree of
Master of Science

June 2020

THESIS APPROVAL PAGE

Student: Maria McQuillan

Title: Modelling Fluid Resonance in Conduit-Crack Coupled Systems: An Application to Englacial Geometries

This thesis has been accepted and approved in partial fulfillment of the requirements for the Master of Science degree in the Department of Earth Sciences by:

Leif Karlstrom	Chair
Alan Rempel	Core Member
Valerie Sahakian	Core Member
Josh Roering	Institutional Representative

and

Kate Mondloch	Dean of the Graduate School

Original approval signatures are on file with the University of Oregon Graduate School.

Degree awarded June 2020

THESIS ABSTRACT

Maria McQuillan

Master of Science

Department of Earth Sciences

June 2020

Title: Modelling Fluid Resonance in Conduit-Crack Coupled Systems: An Application to Englacial Geometries

Englacial structures are an integral part of the glacial hydrological system, yet the internal structure of ice sheets and glaciers remain largely unknown. Resonance of fluids in cracks and conduits has been widely leveraged to infer the geometry of subsurface transport networks, but has not seen a wide application to glaciology. The range of possible englacial geometries is not well constrained. Therefore we explore a range of possible crack geometries, including symmetric and asymmetric tabular cracks that may intersect a conduit at an arbitrary angle. We define the resonant modes as a function of geometry and study which modes are excited for a given impulse forcing at the conduit surface. We find that a coupled mode between the conduit and crack as well as Krauklis wave mode, if detectable, constrain the geometry of hidden cracks. We finally interpret published data from fracture resonance in the glacial system according to our model.

CURRICULUM VITAE

NAME OF AUTHOR: Maria McQuillan

GRADUATE AND UNDERGRADUATE SCHOOLS ATTENDED:

University of Oregon, Eugene, OR, USA
University of Saint Thomas, Saint Paul, MN, USA

DEGREES AWARDED:

Master of Science, Earth Sciences, 2020, University of Oregon
Bachelor of Science, Physics, 2017, University of Saint Thomas

AREAS OF SPECIAL INTEREST:

Glaciology
Fluid Dynamics

PROFESSIONAL EXPERIENCE:

Heliophysics Intern, NASA Goddard Space Flight Center, 2016
Annual Instructor, Dept. of Physics, University of Cincinnati, 2017-2018

GRANTS, AWARDS AND HONORS:

Barry Goldwater Award, 2015
John Mather Nobel Scholar Award, John and Jane Mather Foundation for Science and the Arts, 2016
Graduate School Promising Scholar Award, University of Oregon, 2018

ACKNOWLEDGEMENTS

I wish to express sincere appreciation to my advisor Dr. Leif Karlstrom and my committee Dr. Alan Rempel and Dr. Valerie Sahakian for their assistance in the preparation of this manuscript. In addition, special thanks are due to Dr. Brittany Erickson who provided invaluable insight and emotional support throughout this undertaking.

TABLE OF CONTENTS

Chapter Page

LIST OF FIGURES

LIST OF TABLES

Table Page

CHAPTER I

INTRODUCTION

The englacial hydrological system modulates water transport from the supraglacial environment to the subglacial system, however little is known about the geometry of these water transport pathways. The geometry of these pathways could dramatically impact the efficacy of water transport to the glacier base (Fountain et al. 2005), which subsequently impacts the rate at which water is introduced to the subglacial system (Banwell et al. 2016, Schoof et al. 2010). In this study we investigate how fluid resonance may be used to interrogate these hidden water transport pathways.

The most common methods to probe englacial structures are speleological, ice penetrating radar, or *in situ* observations using boreholes and cameras (Vatne et al. 2001, Catania et al. 2008, Graff et al. 2019). Through these methods we know the englacial system could be composed of fractures, larger conduits or possibly both (Fountain et al. 2005). However, while these methods are useful for identifying features in isolated cases, they are limited in the sizes of features they can identify and often fail to determine the dimensions of such features, which can inform water storage and transport rate. We propose fluid resonance in englacial structures may provide a more versatile and informative approach for defining englacial pathways.

Fluid resonance occurs at distinct frequencies that can be related to excitation mechanisms and the geometry of the resonator. Fluid resonance as a method to define subsurface features has seen wide application in oil and gas exploration, and is beginning to see applications in volcanology (Liang et al. 2020, Holzhausen 1986, Mondal 2010, Molenaar et al. 2012, and others). Specifically,

fluid resonance in fractures has proven powerful for determining fracture lengths and widths which could be invaluable for understanding englacial water transport. Glaciologists have just begun to scratch the surface of these methods (Lipovsky and Dunham 2015, Roeoesli et al. 2016, Graff et al. 2019 and Podosky et al. 2020) and this study aims to further define the limits for which fluid resonance could be used to define simple and complex englacial geometries.

We assume an englacial geometry of a conduit connected to one or more englacial cracks. We then model wave motion in these coupled structures to determine the resulting resonant spectra. We interpret resulting resonant behavior in the context of pre-existing theory for resonance in these geometries and evaluate the limits for which they apply to the englacial environment. Finally we apply our results to a real data set from Rhonegletscher glacier (Graff et al. 2019) in the Swiss Alps and discuss the effectiveness of our methods.

CHAPTER II

MODELLING THE ENGLACIAL SYSTEM

The englacial system can be a complicated active network of fluid or air filled cracks and/or conduits. We assume a simplified englacial geometry as a subvertical tube connected to one or more elastic fractures, as seen in Figure 1. We assume excitation wavelengths are long compared to fracture openings and the conduit radius. This allows us to consider pressures to be uniform in the radial and crack opening directions. Furthermore, we assume elastic deformation occurs much slower than elastic wave speeds in ice and thus the elastic conduit and fracture walls respond quasi-statically to pressure and velocity perturbations, thus we neglect any seismic radiation into the surrounding solid (Krauklis 1962, Ferrazzini and Aki 1987). Finally, we consider fluid flow is fully developed and that there are no changes in density due to bubble or suspended sediment in the water. In the fully developed flow limit we assume the velocity profile can be represented as Poiseuille flow. Our interest is in small perturbations to a static background state, which we excite using an impulsive pressure pulse. Under these assumptions, we use a linearized theory of wave propagation in elastic conduits and cracks, largely following the derivation and numerical implementation in Liang et al. (2020).

Governing Equations: Fluid Filled Conduit

We begin by considering the vertical momentum balance for an unsteady fluid in a cylindrical conduit with radius R and length L. By limiting our study to wavelengths larger than the conduit radius, pressure is uniform in the radial direction (lubrication approximation) and velocity will be axisymmetric,

$$\rho^*(\frac{\partial v^*}{\partial t} + v^*\frac{\partial v^*}{\partial z}) + \frac{\partial p^*}{\partial z} = \mu\frac{1}{r}\frac{\partial}{\partial r}r\frac{\partial v^*}{\partial r} \tag{2.1}$$

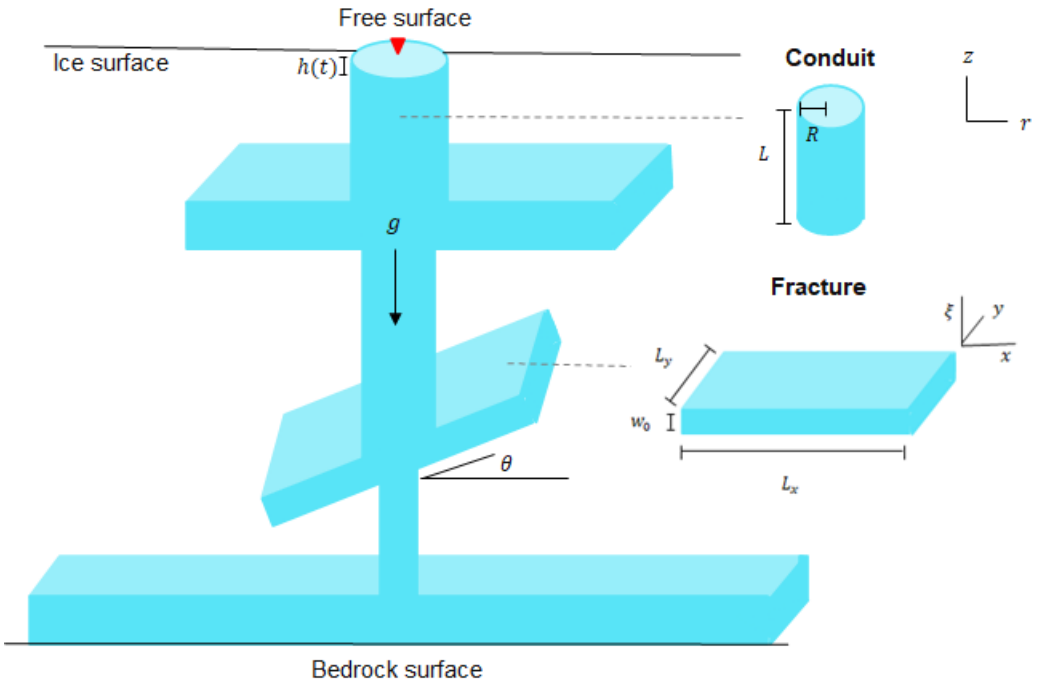

Figure 1. Our model of the englacial system showing multiple fractures. For this study we mostly focus on a system with a single fracture either at the base or in the center of the conduit. Fractures are defined by two crack lengths L_x and L_y and an unperturbed opening w_0. Conduit sections are defined by a length L and a radius R. Fractures may also be dipping at an angle θ with respect to the horizontal axis. The free surface is denoted by a red triangle. h(t) is the height of the water surface in reference to an unperturbed fluid surface.

where v^*, p^* and ρ^* are particle velocity, pressure and density and μ is the dynamic viscosity. Depth, z, is measured from the bottom of the conduit and r is defined as the radial distance from the conduit center. For this study we will focus only on systems in the Poiseuille flow limit where the velocity profile is considered to be parabolic in the conduit (the appropriateness of this assumption will be discussed later). We also assume wavelengths will be much larger than the conduit radius, thus we can consider a cross-sectionally averaged vertical velocity

$$u^*(z,t) = \frac{1}{\pi R^2}\int_0^R v^*(z,r,t)2\pi r dr. \tag{2.2}$$

This simplifies the momentum balance to

$$\rho^*(\frac{\partial u^*}{\partial t} + u^*\frac{\partial u^*}{\partial z}) + \frac{\partial p^*}{\partial z} = -\frac{8\mu}{R^2}u^*. \tag{2.3}$$

To round out the governing equations we present the system mass balance and the Lagrangian equation of state for the fluid using this cross-sectionally averaged velocity

$$\frac{\partial \rho^*}{\partial t} + \rho^*\frac{\partial u^*}{\partial z} = 0, \tag{2.4}$$

$$\frac{1}{\rho}\frac{\partial \rho^*}{\partial t} = \frac{1}{K}(\frac{\partial p^*}{\partial t} + u^*\frac{\partial p^*}{\partial z}), \tag{2.5}$$

where K is the fluid bulk modulus.

Next, we linearize equations (2.3), (2.4) and (2.5) about a static background state to focus on the response of the system to small perturbations. We represent the total fields as a sum of the background state, denoted with an overbar, and a small perturbation

$$[\rho^*, u^*, p^*] = [\bar{\rho} + \rho, \bar{u} + u, \bar{p} + p]. \tag{2.6}$$

The static background state implies

$$\begin{aligned} \bar{u} &= 0, \\ \bar{p} &= constant, \\ \bar{\rho} &= constant. \end{aligned} \tag{2.7}$$

Substituting the expressions in (2.6) and (2.7) into the governing equations and removing non-linear terms in the perturbed quantities results in the following linearized equations

$$\frac{\partial \rho}{\partial t} + \bar{\rho}\frac{\partial u}{\partial z} = 0, \tag{2.8}$$

$$\bar{\rho}\frac{\partial u}{\partial t} + \frac{\partial p}{\partial z} = -\frac{8\mu}{R^2}u, \tag{2.9}$$

$$\frac{1}{\bar{\rho}}\frac{\partial \rho}{\partial t} = \frac{1}{K}\frac{\partial p}{\partial t}. \tag{2.10}$$

We can then combine equations (2.8) and (2.10) to get our simplified governing equations

$$\frac{1}{K}\frac{\partial p}{\partial t} + \frac{\partial u}{\partial z} = 0 \tag{2.11}$$

$$\bar{\rho}\frac{\partial u}{\partial t} + \frac{\partial p}{\partial z} = -\frac{8\mu}{R^2}u. \tag{2.12}$$

It must be noted that these equations are only valid for systems in the fully developed flow limit (Womersley 1955). Assuming fully developed flow simplifies the viscosity term in the vertical momentum balance, but may provide unrealistic viscous damping effect considering the englacial environment. We move forward with this assumption for simplicity (Liang et al 2020) and leave a more rigorous treatment of viscosity to future work.

Boundary Conditions. To supplement the governing equations, we impose no slip boundary conditions on all conduit walls. At the top of the conduit the free surface is allowed to respond freely to atmospheric pressure

$$p(z,t)|_{z=L} = \rho g h(t) \tag{2.13}$$

where h(t) is the fluid surface displacement at the free surface forming the top of the conduit (Fig. 1), and can be calculated using the fluid velocity at the surface

$$u|_{z=L} = \frac{dh}{dt}. \tag{2.14}$$

We treat the bottom of the conduit as a pressure boundary condition to simulate the response of an open fracture connected to the base of the conduit

$$\frac{dp}{dz}|_{z=0} = -C_t A u \tag{2.15}$$

where C_t is the storativity of the crack (discussed below), and $A = \pi R^2$ is the cross-sectional area of the conduit. In the absence of a crack or for short excitation wavelengths, $\frac{dp}{dz} = 0$ and the bottom boundary becomes a constant velocity boundary condition $u = 0$.

Governing Equations: Fluid Filled Crack

For the fracture, we consider a 3D crack with the independent coordinate system x, y, and ξ where x is along dip, y is along strike and ξ represents the direction of opening of the fracture as seen in Figure 1. We begin with the linearized equations for fluid flow in a 3D fracture (Ferrazzini and Aki 1987, Linag et al. 2020)

$$\frac{\partial \rho}{\partial t} + \bar{\rho}\frac{\partial v_x}{\partial x} + \bar{\rho}\frac{\partial v_y}{\partial y} + \bar{\rho}\frac{\partial v_\xi}{\partial \xi} = 0, \tag{2.16}$$

the momentum balance in each direction is,

$$\bar{\rho}\frac{\partial v_x}{\partial t} + \frac{\partial p}{\partial x} = \mu\frac{\partial^2 v_x}{\partial \xi^2}, \tag{2.17}$$

$$\bar{\rho}\frac{\partial v_y}{\partial t} + \frac{\partial p}{\partial y} = \mu\frac{\partial^2 v_y}{\partial \xi^2}, \tag{2.18}$$

and the equation of state in the crack is

$$\frac{1}{\bar{\rho}}\frac{\partial \rho}{\partial t} = \frac{1}{K}(\frac{\partial p}{\partial t} + v_x\frac{\partial p}{\partial x} + v_y\frac{\partial p}{\partial y} + v_\xi\frac{\partial p}{\partial \xi}). \tag{2.19}$$

Similar to the conduit case, we assume Poiseuille flow and due to the assumption that excitation wavelengths will be much longer than crack widths we can

represent these equations in a width averaged description. The width averaged velocities are expressed as

$$u_x(x,y,t) = \frac{1}{w_0}\int_0^{w_0} v_x(x,y,t)d\xi, \tag{2.20}$$

$$u_y(x,y,t) = \frac{1}{w_0}\int_0^{w_0} v_y(x,y,t)d\xi. \tag{2.21}$$

Re-writing our equations in terms of the width averaged description and accounting for Poiseuille flow yields

$$\bar{\rho}\frac{\partial u_x}{\partial t} + \frac{\partial p}{\partial x} = -\frac{12\mu}{w_0^2}u_x, \tag{2.22}$$

$$\bar{\rho}\frac{\partial u_y}{\partial t} + \frac{\partial p}{\partial y} = -\frac{12\mu}{w_0^2}u_y, \tag{2.23}$$

$$\frac{\partial \rho}{\partial t} + \bar{\rho}\frac{\partial u_x}{\partial x} + \bar{\rho}\frac{\partial u_y}{\partial y} + \bar{\rho}\frac{1}{w_0}\frac{\partial w}{\partial t} = 0, \tag{2.24}$$

$$\frac{1}{\bar{\rho}}\frac{\partial \rho}{\partial t} = \frac{1}{K}\frac{\partial p}{\partial t}. \tag{2.25}$$

To close our system of equations we apply no slip boundary conditions to all fracture walls.

$$\begin{aligned} u_x|_{x=0,L_x} &= 0, \\ u_y|_{y=0,L_y} &= 0. \end{aligned} \tag{2.26}$$

Elasticity. We are interested in oscillations related to fracture deformation and thus consider crack elasticity. The elastic response of the crack is solved using a combination of Hooke's Law and the Okada dislocation model

of a mode one fracture an elastic half-space. The crack is modelled as a grid of fracture cells where Okada's solutions are used to calculate the overall "stiffness", K_s, of the crack. This is achieved by imposing a unit opening on each fracture cell and summing the resulting stresses on each cell by every other cell to represent the overall stress field for the fracture as a matrix K_s. Using Hooke's law we can relate this stress field and the internal pressure of the fracture to the resulting fracture opening, w.

$$w = \frac{1}{K_s} p \tag{2.27}$$

In addition to fracture stiffness, we can also use this method to calculate the crack compressibility. The compressibility of a crack is defined as

$$\beta_c = \frac{1}{V_c} \frac{dV_c}{dp_c} \tag{2.28}$$

where $V_c = L_x * L_y * w_0$ is the volume of the crack and p_c is uniform pressure over the boundary of the crack. To calculate dV_c/dp_c we use the stiffness matrix, $\frac{1}{K_s}$, mentioned above to calculate the relative opening for two different arbitrary pressures. We then sum up the openings and multiply by L_x and L_y to calculate the resulting volume for each pressure. Finally, we subtract the two volumes and divide by the change in pressure to obtain fracture compressibility.

Coupling of the Conduit and Crack

Our interest is in resonant behavior in a coupled conduit-crack system. We couple the conduit and crack system of equations through interface conditions on both velocity and pressure at each crack. We impose pressure continuity and a jump condition in the velocity due to the flux into the crack at each crack interface.

$$p(z_c^+, t) - p(z_c^-, t) = 0 \tag{2.29}$$

$$q(z_c^+, t) - q(z_c^-, t) = -A_f u(z_c, t) \tag{2.30}$$

Where q is the volume flow rate above and below the crack, A_f is the area of the crack opening $A_f = 2\pi R w_0$, and z_c is the depth of the crack in the conduit.

Next we incorporate volume flux into the crack and crack elasticity into the governing equations. Assuming wavelengths of the perturbation are long compared to the crack opening and combining equations (2.24) and (2.25) and (2.37) we get

$$\frac{1}{\bar{K}}\frac{\partial p}{\partial t} + \frac{\partial u_x}{\partial x} + \frac{\partial u_y}{\partial y} = \frac{q_c}{w_0}\delta(x - x_c)\delta(y - y_c) \tag{2.31}$$

Where $\frac{1}{\bar{K}}$ is the sum of the fluid and crack compressibility $\frac{1}{\bar{K}} = \frac{1}{w_0 K_{crack}} + \frac{1}{K_{fluid}}$ and q_c is the flux into the crack from the conduit. Additionally, a delta function is implemented at a single coupling point (x_c, y_c) in the fracture. This coupling point is where the center of the conduit intersects the fracture. The right-hand-side term represents a mass source for the fluid exchange between the conduit and the crack, where the delta function is defined as $\delta(x - \alpha) = \frac{1}{2\pi}\int_{-\infty}^{\infty} e^{i\omega(x-\alpha)} d\omega$. This results in a point source excitation of $\frac{q_c}{w_0}$ that radiates from the coupling point.

Numerical Implementation

We solve the coupled system of equations using 6th order summation by parts finite difference operators in space and a 4th-order additive Runge-Kutta method in time (Erickson et al. 2019, O'Reilly et al. 2017). Boundary conditions in the conduit are weakly enforced using simultaneous approximation terms (SAT) and strongly enforced in the crack. The summation by parts method replaces continuous derivatives with discrete operators. The first derivative operator is defined as the inverse of the quadrature matrix, H, multiplied by Q, $D = H^{-}Q$, where Q is an almost skew symmetric matrix defined as $Q + Q^T = diag[-1, 0...0, 1]$.

Summation by parts operators represent a discrete method for integrating by parts allowing us to write a discrete energy balance that mimics the continuous version and thus easily prove time stability and high order accuracy (Fernandez et al. 2014). Simultaneous approximation terms provide a method to weakly enforce boundary conditions in the SBP framework by penalizing the value at the boundary to meet the expected boundary condition (Carpenter et al. 1994). This method enables conservation of energy at interfaces where the solution may be multi-valued (Fernandez et al. 2014). The equations in the conduit are solved on regular collocated grids, while the crack requires velocity grids to be staggered with respect to the pressure grid. This prevents a singularity at the crack center. Additionally, to maintain high-order accuracy, the viscosity terms are solved implicitly in time (Liang et al. 2020).

In this section we will focus only on the equations for the conduit, but the process is very similar for the crack and can be found in Liang et al 2020. Replacing the spatial derivatives with the SBP operators in equations (2.9) and (2.11) and writing the boundary conditions in terms of SAT variables results in the following discretized governing equations for the conduit

$$\frac{\partial u}{\partial t} = -\frac{D}{\bar{\rho}}p + \frac{8\mu}{\bar{\rho}R^2}u - \frac{\sigma_1}{\bar{\rho}}(u_0)e_0 + \frac{\sigma_2}{\bar{\rho}}(u_N)e_N, \tag{2.32}$$

$$\frac{\partial p}{\partial t} = -DKu + K\sigma_3(Zu_0)e_0 + K\sigma_4(Zu_N)e_N, \tag{2.33}$$

where u_0 and u_N are velocities at the boundary, e_0 and e_N are matrices of the form diag[1,0,0...] and diag[...0,0,1], and Z is the acoustic impedance $Z = \rho c$.

Using the discrete equations (2.32) and (2.33) we can prove stability at high order accuracy by proving the energy of the system is always decreasing at the boundaries. We begin with the continuous energy balance for the conduit. We

multiply equation (2.11) by pressure, p and multiply equation (2.9) by velocity, u, integrate over the entire conduit and sum the two resulting equations to get

$$\frac{d}{dt}\left(E_{pipe} - E_{visc}\right) = \frac{d}{dt}\left(\int_0^L \frac{\bar{\rho}u^2}{2}dz + \int_0^L \frac{p}{2K}dz\right), \tag{2.34}$$

where $E_{visc} = \int_0^L \frac{8\mu}{R^2}u^2 dz$ and represents uniform viscous damping. The discrete energy balance follows a similar method to the continuous problem. We multiply equation (2.33) by $p^T H$ where H is the quadrature matrix for discrete integration, and multiply equation (2.32) by $u^T H$. We then transpose and sum the two equations and use the product rule $d(a^T Ha)/dt = a^T H(da/dt) + (da^T/dt)Ha$ to obtain the discrete energy balance. The left hand side of this equation is

$$\frac{d}{dt}\left(E_{pipe} - E_{visc}\right) = \frac{d}{dt}\left(\frac{\rho}{2}u^T Hu + \frac{1}{2K}p^T Hp\right) \tag{2.35}$$

and the right hand side including the boundary conditions becomes:

$$\frac{d}{dt}\left(E_{pipe} - E_{visc}\right) = p_0 u_0 + \sigma_1 u_0^2 + +\sigma_3 Z u_0 p_0 - p_N u_N + \sigma_2 u_N^2 + \sigma_4 Z p_N u_N \tag{2.36}$$

where σ_1, σ_2, σ_3 and σ_4 are the SAT penalty terms which are chosen to ensure $\frac{dE_{pipe}}{dt}$ is always decreasing. These terms are chosen to be

$$\begin{aligned} \sigma_1 &= -Z, \\ \sigma_2 &= -Z, \\ \sigma_3 &= -c/K, \\ \sigma_4 &= -c/K. \end{aligned} \tag{2.37}$$

Excitation

We generate wave motion in the system using an impulsive pressure pulse. In the englacial setting it is likely that natural excitation could come from both impulsive, or continuous sources. Roeoesli et al 2016 observed resonant phenomena likely occurring from a continuous source, water entering a moulin. However, Graff et al 2019 describe impulsive excitation of crack wave modes in the basal water

layer. We focus on the impulsive case for this study and use a Gaussian pressure pulse to perturb our system

$$f_{source} = A_g e^{-\frac{t^2}{2}}, \tag{2.38}$$

where A_g is the amplitude of the Gaussian pressure signal. Figure 2 shows the Fourier transform of our source function, where the Fourier transform and it's inverse are defined as

$$\begin{aligned} g(\omega) &= \frac{1}{2\pi}\int_{-\infty}^{\infty} f(t)e^{-i\omega t}dt, \\ f(t) &= \int_{-\infty}^{\infty} g(\omega)e^{i\omega t}d\omega, \end{aligned} \tag{2.39}$$

and $\omega = 2\pi f$, where f is frequency. In Figure 2, We see the Gaussian pressure pulse produces a large range of frequencies which can in-turn excite a broad spectrum of modes. We define a wavelength scale for the Gaussian function to be $\lambda_{ex} = \frac{c}{\Delta f_{FWHM}}$ where Δf_{FWHM} is the full width at half maximum of the Gaussian in the Fourier domain. Different excitation functions can be used to broaden the input frequency range, such as a chirp signal, but for simplicity we will only use a Gaussian signal for this study.

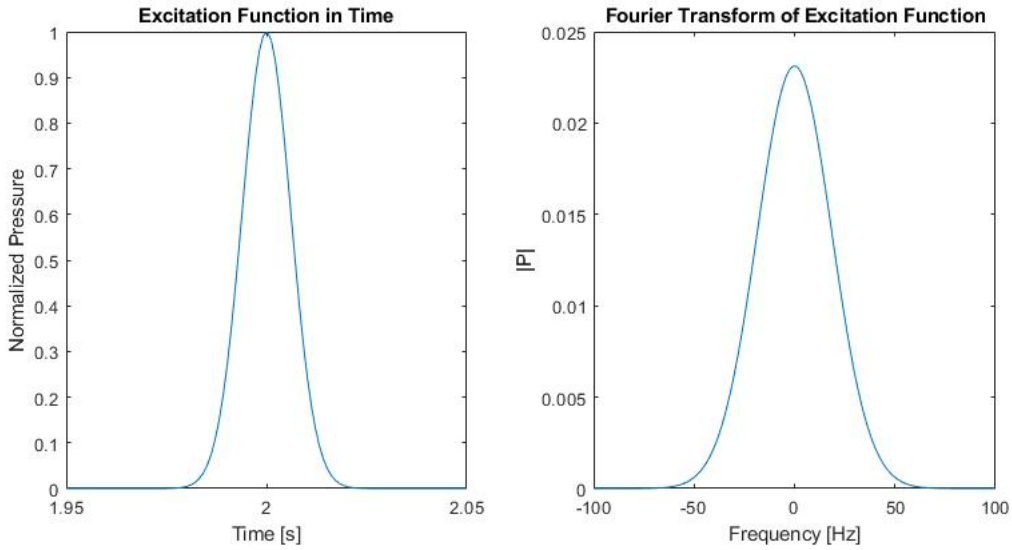

Figure 2. Figure showing the time domain and Fourier domain plots of the excitation function with a wavelength $\lambda_{ex} = \frac{c}{\Delta f_{FWHM}}$, where $c = 1400$ is the wave speed, $\lambda_{ex} = 20m$ and Δf_{FWHM} is the FWHM of the gaussian in the Fourier domain. The excitation function in time for this example is $f(t) = e^{\frac{-1}{2}(\frac{(t-2)}{0.0061})^2}$

CHAPTER III

WAVE MOTION AND RESONANCE

There are many different resonant modes that can be excited in our modelled system. In this section we discuss how we can use pre-existing theory to help identify the origin of these resonant modes in our tested geometries. We will focus on two types of interface waves that may resonate in the englacial system, tube waves and crack waves.

Conduit and Fracture Components

Tube waves manifest from fluid solid interactions in fluid filled tube-like geometries. In general, the dynamic elasticity of the tube excites non-local interface waves, such as Stonely waves, psuedo-Rayleigh waves, and Airy phase waves, that manifest from high frequency excitation and pressure changes in the radial direction (Sheriff 1987.). For low frequency excitation, wall deformation occurs on time scales much longer than tube wave propagation speeds and the walls can be considered to deform quasi-statically. This results in a local response between the solid and the fluid in the form of compressional waves. This tube wave is non-dispersive and travels in the fluid at a slightly slower speed than the acoustic wave speed. For a circular borehole, this speed is modulated by the shear modulus of the surrounding elastic solid, the bulk modulus of the fluid and the fluid density (Biot 1952).

$$c_T = \sqrt{\frac{1}{\rho}\left(\frac{1}{K} + \frac{1}{G}\right)^{-1}} \tag{3.1}$$

Compressional tube waves, like acoustic waves in a cylindrical pipe, will resonate at "organ pipe" frequencies. Where the resonant modes depend on the tube wave speed, the boundary conditions – whether the ends of the pipe are open or closed –

and the conduit length (Lighthill 2010).

$$f_{open/open} = \frac{nc_T}{4L} \tag{3.2}$$

$$f_{open/closed} = \frac{nc_T}{2L} \tag{3.3}$$

where n is a positive integer denoting the mode harmonic, c_T is the tube wave speed and L is the length of the pipe.

Crack waves, or Krauklis waves, are a type of guided interface wave that manifests in fluid filled fractures. Crack waves result from coupled fluid and elastic solid motion and are excited when wavelengths exceed an elastic coupling limit (Krauklis 1962, Ferrazzini and Aki 1987, Dunham and Ogden 2012). This limit is defined as

$$\Lambda_{el} = \frac{\beta_c}{\beta_f}, \tag{3.4}$$

where β_c is the compressibility of the crack and β_f is the compressibility of the fluid. When $\Lambda << 1$ wavelengths are too short and the fracture will respond rigidly. In this case, acoustic resonant frequencies can be calculated using the following expression (Rona 2007): $f_{l,m,n} = c\sqrt{(\frac{l}{2L_x})^2 + (\frac{m}{2L_y})^2 + (\frac{n}{2w_0})^2}$. Where l,m and n are positive integers denoting the mode harmonics. L_x, L_y and w_0 are the crack dimensions in x, y, and z directions respectively and c is the acoustic wave speed.

When $\Lambda >> 1$ excitation wavelengths are long enough for the fracture to be compliant and crack waves will manifest. Crack waves are dispersive, meaning the speed at which the wave travels depends on the wavelength. This manifests as unequal spacing of resonant harmonics in the Fourier domain. The complex dispersion of crack waves also leads to complicated transcendental equations that must be solved numerically to predict the wave speed and resonant frequencies.

We employ a fracture transfer function derived in Liang et al 2017, to predict crack wave resonant frequencies

$$F(\omega) = \frac{\rho c / A_f}{Z_f(\omega)}, \tag{3.5}$$

where $A_f = 2\pi w_0 R$ is the area of the fracture opening and $Z_f(\omega)$ is the fracture impedance which can be calculated by Fourier transforming the fluid flux and pressure time series at the fracture mouth

$$Z_f(\omega) = \frac{\hat{p}(0,\omega)}{A_f \hat{u}(0,\omega)}. \tag{3.6}$$

Frequencies where the amplitude of the fracture transfer function is maximized or minimized represent the resonant modes of crack waves as seen in panel (c) of Figures 4, 8 and 10.

Coupled Geometries

In addition to fracture and tube wave modes, coupled modes exist in this system between the conduit and crack. We focus on a coupled mode between a basal crack and a conduit, referred to in Liang 2020 as the "Conduit Reservoir mode". We will refer to this mode as the "coupled mode" for the remainder of this work. For the coupled mode, fluid is considered incompressible in the conduit and the whole fluid column oscillates in the conduit due to forcing from the elastic crack and gravity from the free surface. Liang 2020 derived this resonant frequency accounting for fluid buoyancy due to density gradients throughout the conduit. While water in glaciers may be very bubbly or filled with sediment, we neglect density changes for our model and derive a simpler expression for the coupled mode.

Starting from our linearized momentum balance in the conduit, we integrate (2.9) in z from 0 to L, and assume the fluid is incompressible

$$\rho\frac{\partial u}{\partial t} + \frac{1}{L}[p_L - p_0] = -\frac{8\mu}{R^2}u. \tag{3.7}$$

The pressure at the surface is $p_L = \rho g h$. For very long wavelengths we can neglect fluid inertia and viscous dissipation in the fracture, then the pressure at the crack interface becomes

$$p_0 = -\frac{Ah}{C_t} \tag{3.8}$$

Where C_t is the storativity of the crack. Storativity is generally expressed in terms of the fluid and crack compressibilty

$$C_t = (\beta_f + \beta_c)V_c \tag{3.9}$$

The compressibility of water is significantly small compared to the icy crack compressibility, about 5 orders of magnitude smaller. If we neglect fluid compressibility, and substitute equation (2.28) into equation (3.9) we get the following

$$C_t = \frac{dV_c}{dp_c} = \kappa\frac{L_x^3}{G^*} \tag{3.10}$$

Additionally storativity of a square fracture can be represented in terms of the effective shear modulus $G^* = G/(1-\nu)$ of ice where G is the shear modulus ice and ν is Poisson's ratio for ice, as well as crack length and a constant kappa. κ depends on the aspect ratio of the crack and must be calculated numerically by calculating $\frac{dV}{dp}$ and solving equation (3.10) for κ. This relationship shows that storativity should scale as the crack length cubed for equal dimension fractures. For glacial parameters, we calculate $\kappa = 0.56388$ by fitting the results of stroativity vs crack length with cubic function and multiplying the coefficient of the cubic term by G^*.

If we substitute equations (3.8) and (2.12) into equation (3.7) we get

$$\rho\frac{\partial u}{\partial t} = -\frac{h}{L}(\rho g + \frac{A}{C_t}) - \frac{8\mu}{R^2}u \tag{3.11}$$

we then divide through by ρ, substitute in equation (2.13) and neglect viscosity to obtain the equation of a simple harmonic oscillator

$$\frac{d^2h}{dt^2} = -\frac{g}{L}(1 + \frac{A}{\rho g C_t})h \tag{3.12}$$

with an inviscid frequency of

$$f_{CR} = \frac{1}{2\pi}\sqrt{\frac{g}{L}(1 + \frac{A}{\rho g C_t})} \tag{3.13}$$

While the coupled mode is derived solely for a crack intersecting at the base of a conduit, this mode can arise in a system with a crack intersecting anywhere along the conduit. However energy from the incoming waves will be partitioned between the fracture and the conduit based on the relative cross-sectional areas of the fracture opening and the conduit. It is standard to express this energy exchange in terms of reflection and transmission coefficients (Lighthill 2010). For our system we use reflection and transmission coefficients derived in Liang et al. 2017.

$$R(\omega) = -\frac{1}{1 + 2/r(\omega)} \tag{3.14}$$

$$T(\omega) = -\frac{2/r(\omega)}{1 + 2/r(\omega)} \tag{3.15}$$

with

$$r(\omega) = -\frac{\rho c_T/A}{\rho c_0/A_c}F(\omega) \tag{3.16}$$

where $A = \pi R^2$ is the area of the conduit and $Ac = 2\pi w_0 R$ is the area of the fracture opening. These reflection and transmission coefficients determine which wavelengths will transmit past the crack and which will interact with the fracture.

If a fracture is dipping at some angle θ the cross-sectional area of the conduit at the fracture interface becomes elliptical and this area change will impact reflection and transmission. For simplicity we account for this area change using an effective circular radius. This method for accounting for fracture dip was first utilized in Tang and Cheng 1993. If we consider the semi-minor axis of the ellipse equal to the conduit radius, the semi-major axis would be

$$R_1 = \frac{R}{cos(\theta)} + \frac{w_0 \tan(\theta)}{2} \tag{3.17}$$

using the ellipticity,

$$e = \sqrt{R_1^2 - R^2/R_1} \tag{3.18}$$

we can write the effective radius as,

$$R_e = \frac{2}{\pi R_1 E(e, \frac{\pi}{2})} \tag{3.19}$$

where $E(e, \frac{\pi}{2})$ is the complete elliptic integral of the second kind: $E(\phi, k) = \int_0^\phi \sqrt{1 - k^2 sin^2(\theta)} d\theta$. Figure 3 shows how the effective radius scales with fracture dip. The largest area changes occur after a dip angle of 70^o. Fractures in the englacial environment have been observed dipping at angles near vertical, which could impact resulting fluid resonance (Fountain et al. 2005).

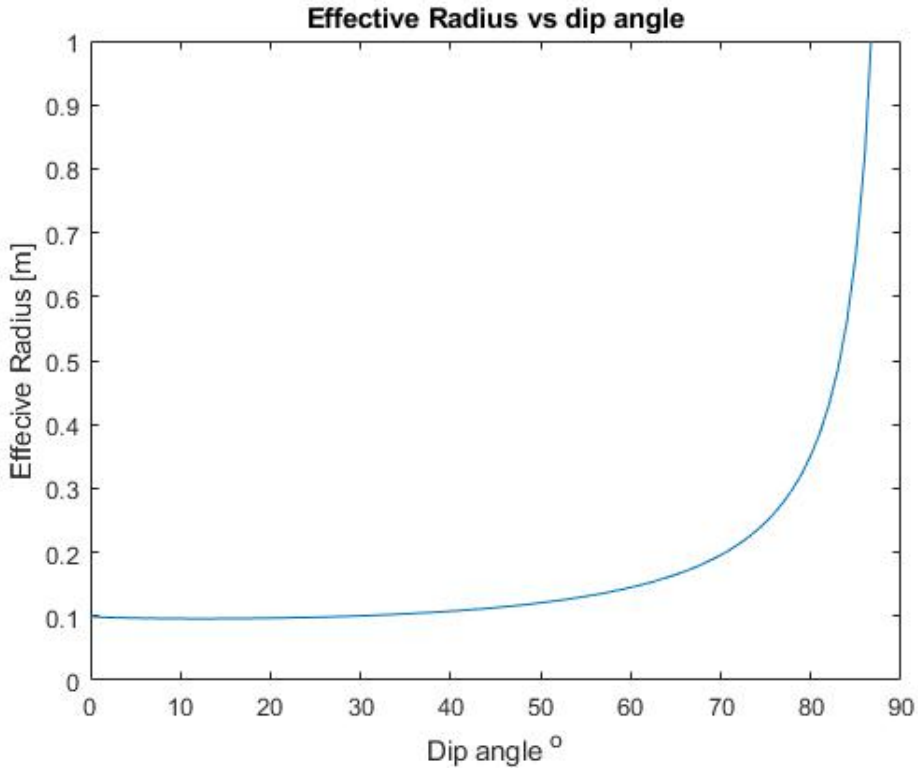

Figure 3. How effective radius scales with crack dip angle (equation (3.19)). Showing a sharp increase in effective radius as the fracture dip exceeds 70^o

CHAPTER IV

RESULTS

In this section we present the results for modelled wave motion in three englacial geometries. We first looked at an englacial geometry with a conduit connected to a basal crack, then a geometry with a conduit connected to a crack located somewhere between the surface and the base and finally a multi-crack system. We excite wave motion in these systems by initiating a pressure pulse at the water surface, then record pressure and velocity time series at locations in the conduit and in the crack. We then Fourier transform these time series to obtain the resonant frequencies in the system. All model parameters for our englacial system can be found in Table 1 and were informed by observations of conduits and fractures in the englacial system (Fountain et al 2005, Catania 2008, Vatne 2001).

Single Crack Geometries

The simplest coupled geometry is a conduit connected to a crack at its base. Figures 4, 5, 6, and 7 show the results from a system with a conduit of length of 100 m, a radius of 0.1 m, a crack length of 5 m in x and y, and a crack opening of 0.01 m. These parameters were chosen to highlight a case where crack waves are high amplitude in the conduit, which we assume is ideal for observation in the field. However, it should be noted that most englacial parameters for this geometry result in much lower amplitude crack waves.

Figure 4 shows the spectral results for this system where we highlight the resulting resonant modes and use pre-existing theory to identify their origin. The red bar in Figure 4 highlights the fundamental mode at 0.75 Hz. This resulting frequency is equivalent to the predicted coupled mode calculated using equation (3.13). The next mode in the spectra is can be identified as the fundamental organ

Table 1. Model Parameters for the englacial setting

Parameter Symbol	Name	Value	Units
L	conduit length	100 - 1000	m
R	conduit radius	0.01 - 0.1	m
L_x	crack length in x	1 - 100	m
L_y	crack length in y	1 - 100	m
w0	crack width	1 - 200	mm
ρ	fluid density	1000	kg/m^3
K	fluid bulk modulus	1.98	GPa
μ	viscosity	$1.8x10^{-3}$	$Pa.s$
ρ_s	solid density	917	kg/m^3
G	shear modulus	3.5	GPa
ν	Poisson's ratio	0.31	-
c_T	tube wave speed	1125	m/s
c_0	acoustic wave speed	1400	m/s

pipe mode at 5.6 Hz. Additionally, higher order harmonics of this mode can be seen at equally spaced intervals from the fundamental organ pipe mode. This organ pipe mode is associated with a pipe open at both ends due to the matching pressure boundary conditions at the conduit surface and base. Finally, the grey bars highlight crack wave resonant frequencies associated with fracture transfer function minima that are detectable both in the crack and the conduit at about 41 Hz, 68 Hz and 103 Hz. Next, we look at the space-time domain results in Figures 5 and 6 and show the complexity of wave motion in this simple system. In Figures 5 and 6 we can see all excited wave modes that were identified in the frequency domain. The initial pressure pulse excitation occurs at the top of the conduit at 2 seconds and at a wave speed of 1125 m/s the tube waves reach the crack at 100 m at about 2.1 seconds. When the pressure pulse reaches the crack, some energy is reflected and some is transmitted into the fracture. This energy is then emitted as crack waves from 2.1 seconds to 2.3 seconds. From 2.6 seconds to about 3.9 seconds we see the coupled mode with a period of about 1.3 seconds. The coupled

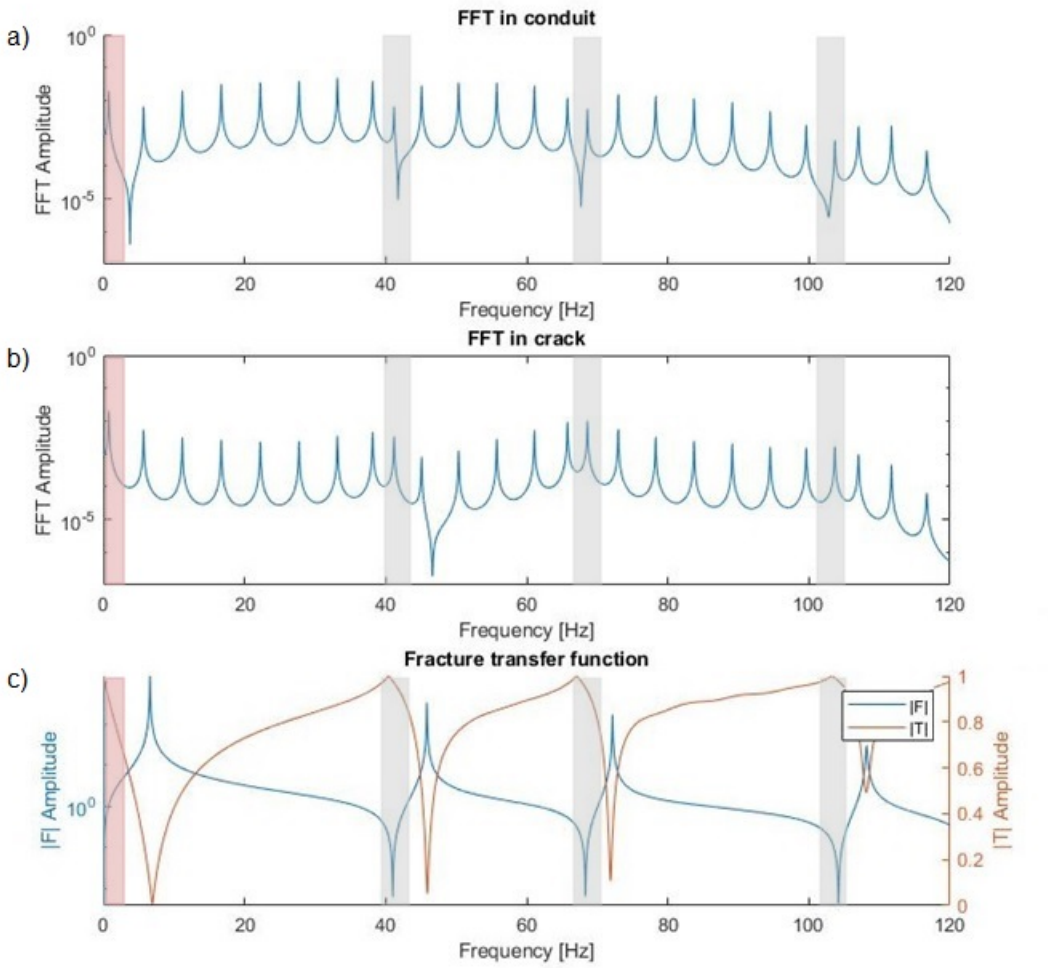

Figure 4. Spectral results for a basal crack with $L = 100$ m, $R = 0.1$ m, $L_x = L_y = 5$ m, $w_0 = 0.01$ m, and a excitation wavelength of 10 m. Panel (a) shows the Fast Fourier Transform of a pressure time series taken halfway down the conduit. Red bars indicate the coupled frequency at 0.75 Hz. The grey bars show crack wave modes at frequencies 41 Hz, 68 Hz and 103 Hz. All other modes are organ pipe modes corresponding to a pipe open at both ends. Panel (b) shows the Fast Fourier Transform of a pressure time series taken just inside the crack. Panel (c) shows the amplitudes of the fracture transfer function, $|F|$, and transmission coefficient, $|T|$, for this crack. We see frequencies of the crack waves in the crack and conduit match the minima in the fracture transfer function.

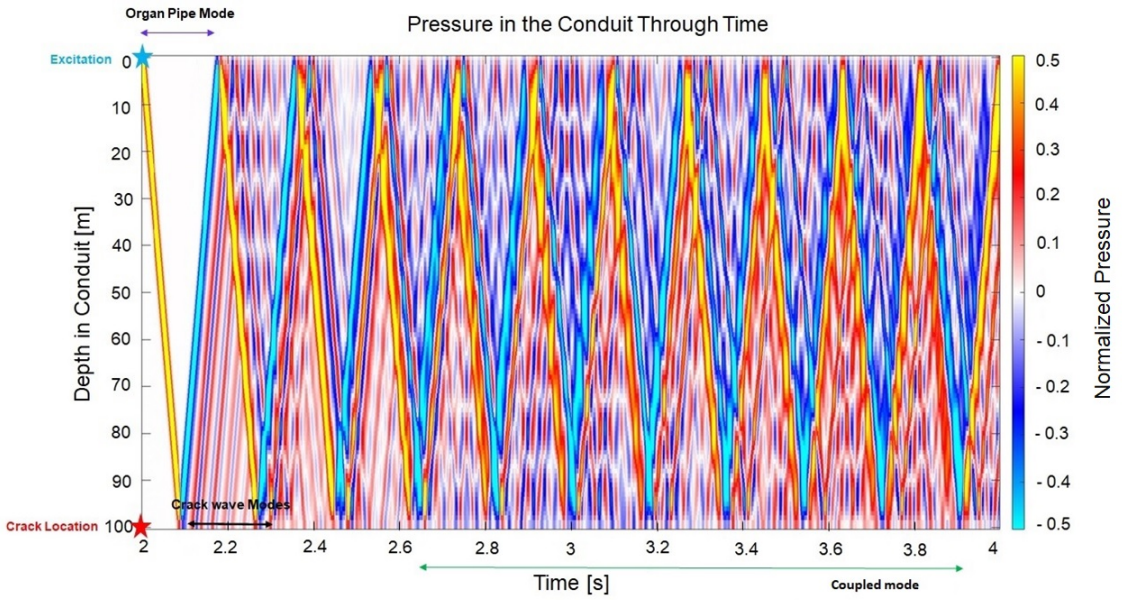

Figure 5. Pressure changes throughout the conduit in time are shown in this space-time plot for the same englacial geometry as Figure 4. Pressure is normalized to atmospheric pressure and is shown on the color bar. Excitation occurs at the top of the conduit at 2 seconds and the crack location is at 100 m. Visible modes in this figure include organ pipe modes, crack wave modes and the coupled mode. Crack waves are first excited at about 2.1 seconds. The coupled mode is best seen by observing the blue to red pressure transitions around the bottom of the plot.

mode is challenging to see in Figures 5 and 6, but is more obvious when looking at the pressure in the crack in Figure 7. Figure 7 shows a horizontal slice of the crack where the center of the crack is at 2.5 m. In this figure the transition from negative pressures from 2.6 to 3.3 to positive pressures from 3.3 to 3.9 represent a full wave period for the coupled mode. We are thus able to identify and explain all resulting resonant wave behavior for the basal crack geometry using our knowledge from pre-existing theory.

We next consider how the coupled mode varies over the full range of englacial parameters seen in Figure 8. Panel (a) shows how the coupled mode varies with conduit length and crack length. For $\gamma = \frac{A}{\rho g C_t} < 1$ we see the coupled

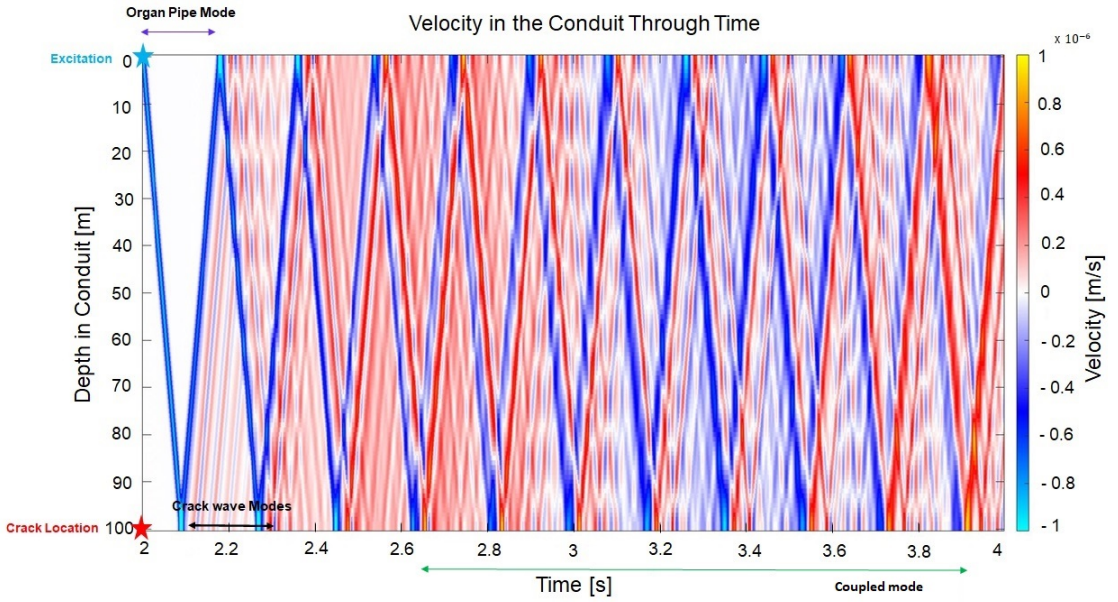

Figure 6. Similar to Figure 5, we show velocity changes throughout the conduit in space and time.

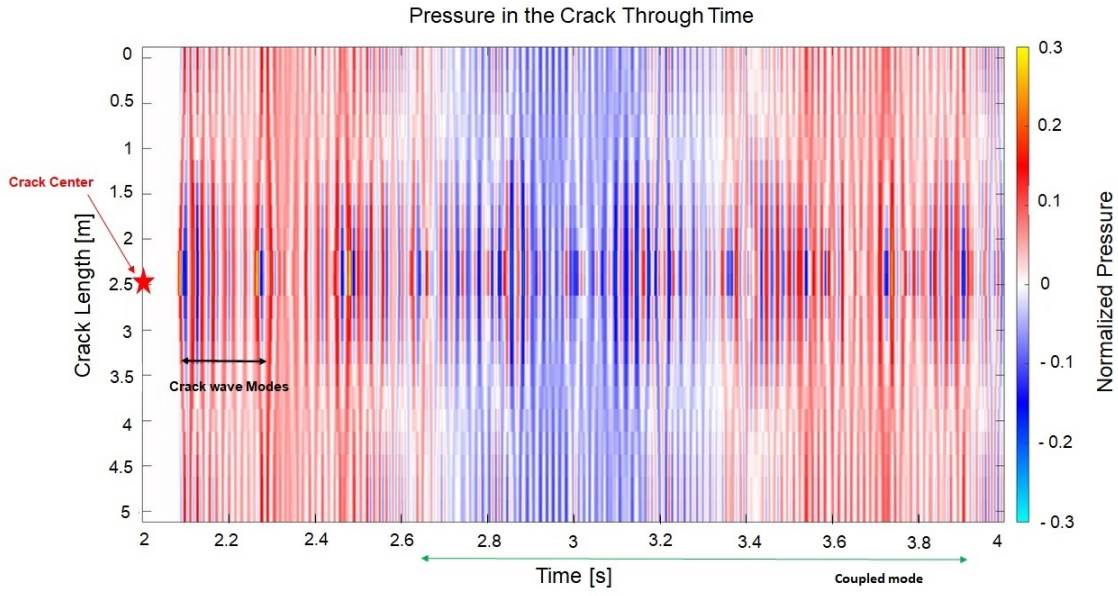

Figure 7. Pressure changes in the crack through space and time. Pressure is normalized to atmospheric pressure and is shown on the color bar. The crack center is located at 2.5 m. Pressure pulses from the conduit are initiated here. The coupled mode is most easily visible in this figure, as we see a distinct 1.3 second period of large scale pressure fluctuations.

mode strongly depends on the crack length. For $\gamma >> 1$ we see the coupled mode no longer depends on crack length and only varies in conduit length. Panels (b) and (c) show how the coupled mode changes with conduit radius. Here we see the coupled mode increases with increasing conduit radius, and we also see an increase in radial dependence as crack length increases.

The fundamental mode for the basal crack geometry will likely always be the coupled mode. To this extent we investigate the limits for which this mode can provide geometric information. Equation (3.13) has two distinct limits. When $\gamma = \frac{A}{\rho C_t g} >> 1$ the frequency for the fundamental mode does not depend on gravity and instead equals $f_{el} = \frac{1}{2\pi}\sqrt{\frac{A/\rho C_t}{L}}$. For $\gamma << 1$, equation (3.13) reduces to a gravity dependent limit, $f_g = \sqrt{g/L}$ where fracture elasticity no longer dominates the system. Figure 9 shows how the coupled mode scales for the full range of englacial parameters described in Table 1. The x-axis of Figure 9 is λ_{el}/L where $\lambda_{el} = c/f_{el}$. For $x < 1$ we see the data collapse onto the elastic frequency limit indicating the data lie within the elastically dominated regime. This is followed by a transition regime at x = 1 where γ is about equal to 1. Finally for $x >> 1$, the data collapse onto the gravity dependent frequency f_g plotted as the dashed lines in Figure 9. The gravity dominated limit does not depend on crack parameters and thus it is not possible to determine crack geometry when in this limit.

Next we look at a case where the crack is no longer at the base of the conduit, but somewhere in the middle. Using the same conduit and crack parameters, we place a crack at about 30 m from the base of the conduit. Figure 10 shows the spectral results for this geometry. We see similar results to the basal crack geometry except with a conduit section above and below the crack, we see more organ pipe modes excited. The organ pipe mode associated with

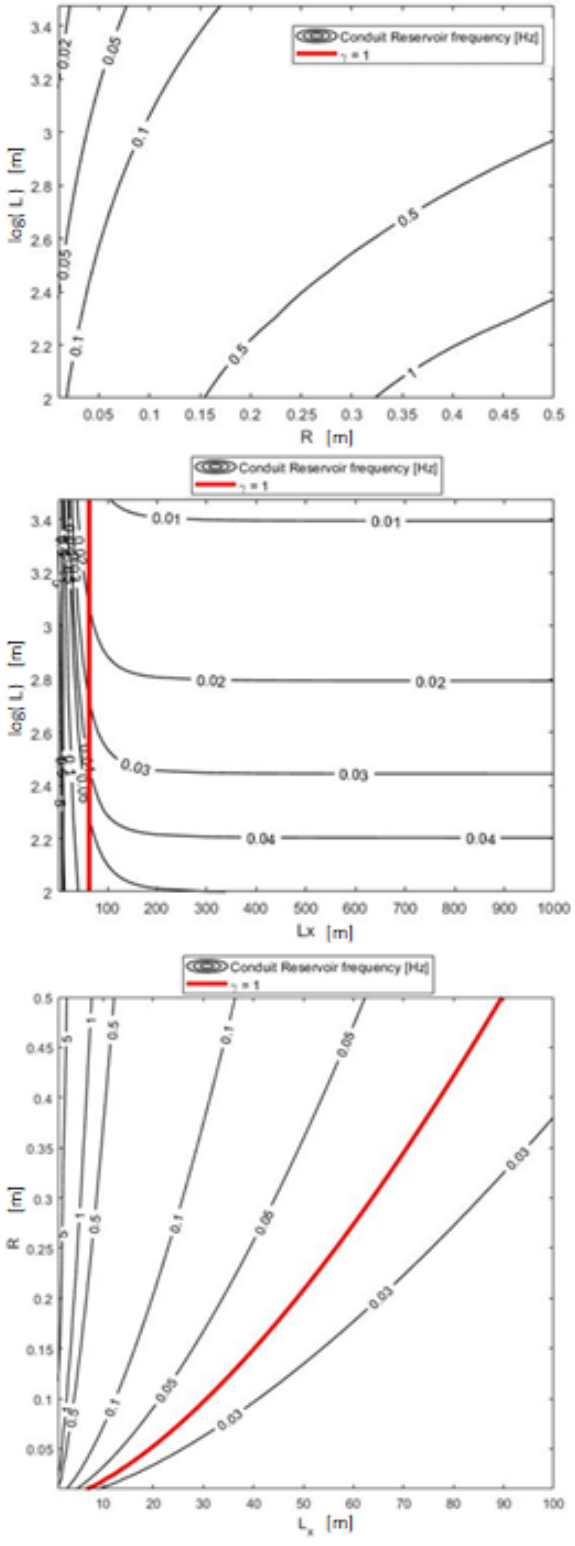

Figure 8. Contours showing the predicted coupled mode for different crack lengths, conduit lengths and radii. The red lines represent where $\gamma = \frac{A}{\rho g C_t} = 1$.

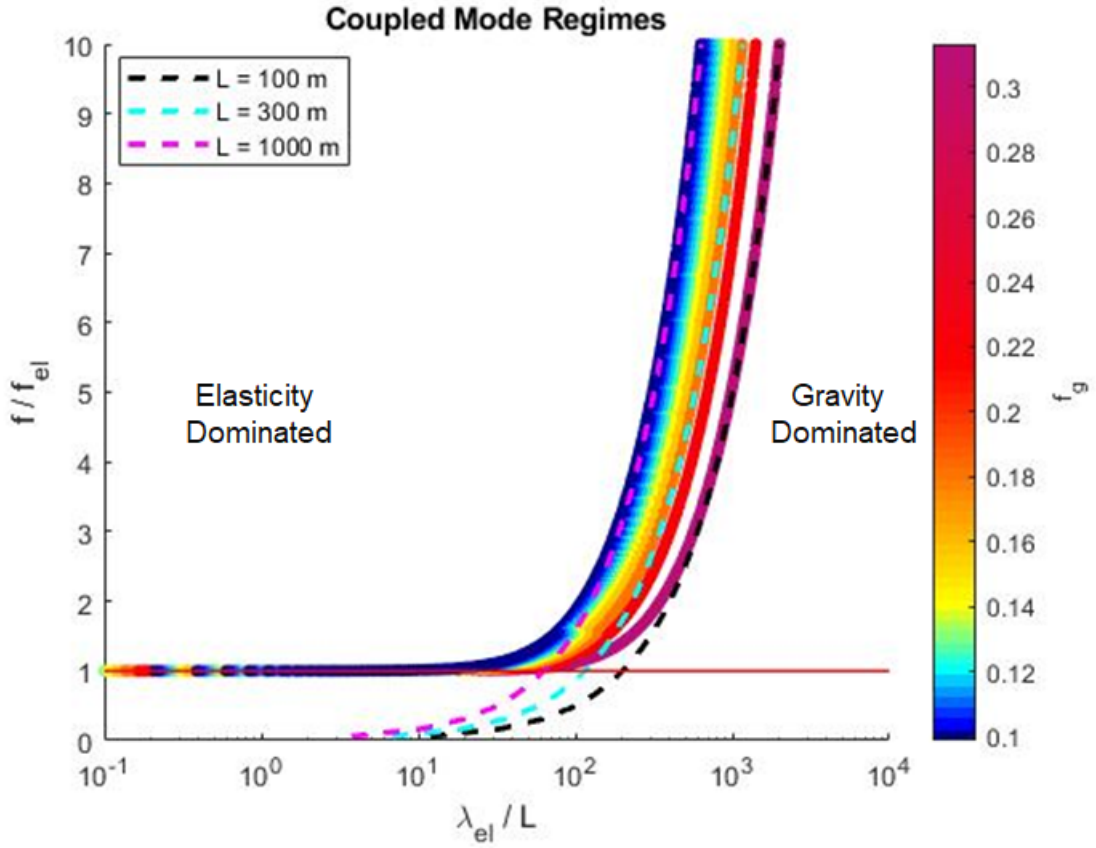

Figure 9. Plots showing how the driving forces of the coupled mode change through the glacial parameter space. The red line represents where f/f_{el} where $f_{el} = \frac{1}{2\pi}\sqrt{\frac{A/\rho C_t}{L}}$. The dashed lines represent the , $f_g = \frac{1}{2\pi}\sqrt{\frac{g}{L}}$ for conduit lengths of 100 m (black), 300 m (cyan) and 1000 m (magenta). The x axis shows the elastic wavelength $\lambda_{el} = c/f_{el}$ normalized by the conduit length

the top conduit section is about 8 Hz and has the largest amplitude above the crack. This frequency is associated with a pipe open at both ends. The organ pipe frequency associated with the bottom conduit section is about 9 Hz, and is equivalent to a pipe open at one end and closed at the other. This is due to the no slip boundary condition at the conduit base. The red bar in panel (b) highlights the coupled mode for the top section of the conduit plus the crack. We do not see a coupled mode associated with the bottom section of the conduit due to the differing boundary conditions. The coupled mode requires a free moving surface to manifest, so the no slip boundary condition at the conduit base prevents this mode from being excited in this conduit section. Finally, the grey bars in panels (b) and (c) of Figure 10 show that the crack wave modes predicted by the fracture transfer function are still represented in the conduit for this geometry.

So far we have only considered fractures parallel to the surface, however, englacial fractures are often observed to be dipping at fairly steep angles (Fountain et al. 2005). Figure 11 shows how dip angle affects the flux into the crack, represented by the reflection coefficient. Figure 11 is considering the same crack geometry as in figure 10. The fracture transfer function for this crack is shown in panel (c) of Figures 4, 10 and 13. Panels (a) and (b) of Figure 11 show that overall the reflection coefficient decreases for increasing dip angle, especially for angles greater than 70^o. The amount for which the reflection coefficient is reduced depends on the fracture transfer function. A decrease in reflection and increase in transmission reduces the total amount of energy interacting with the fracture and thus may decrease the amplitude of fracture related modes. Additionally, an increase in transmission amplifies the fundamental organ pipe mode and suppresses higher order organ pipe modes when the fracture is located in the

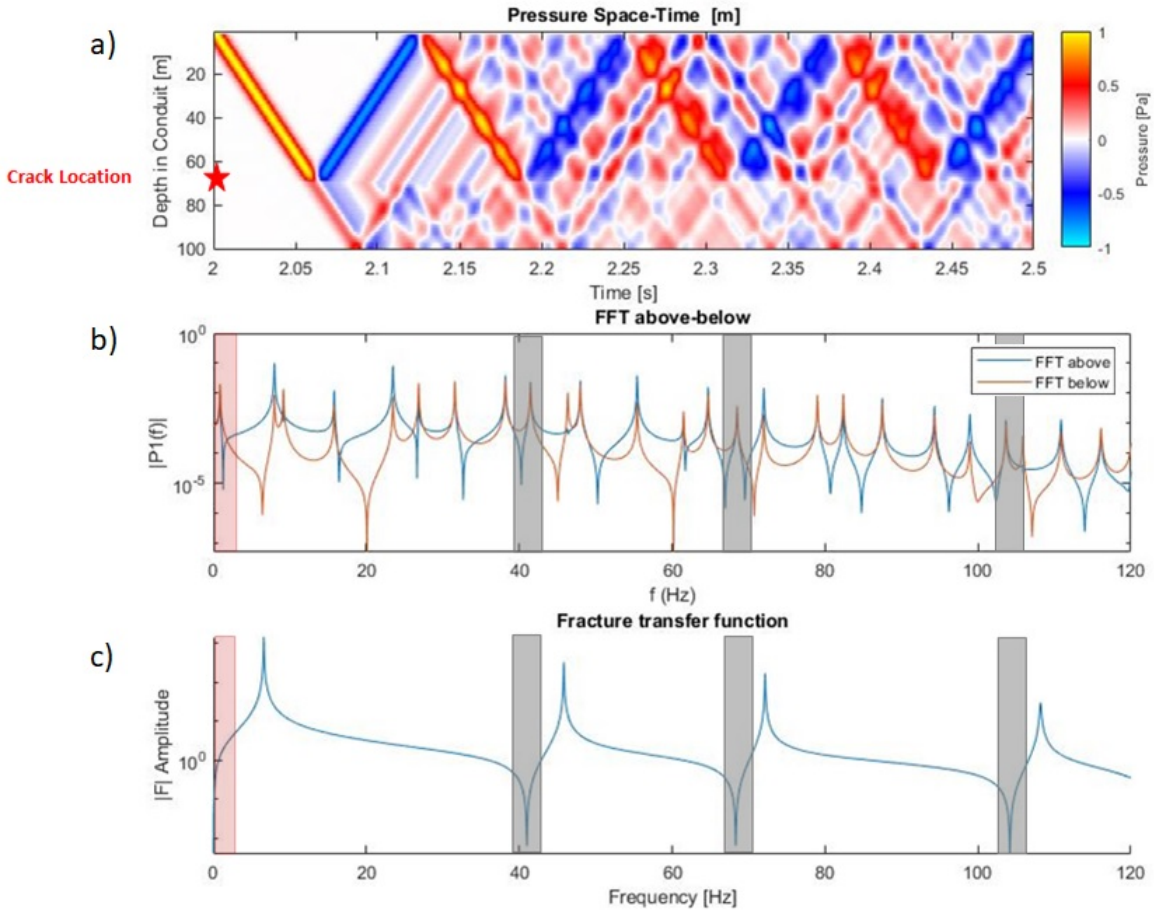

Figure 10. Results for the a crack conduit system with similar parameters to the basal crack system, except the crack is located about 70 m down the conduit rather than at the base. Panel (a) shows pressure changes through the conduit in time. The crack location is marked with a red star. Panel (b) shows the Fast Fourier Transform of two pressure time series, one above the crack at about 35 m down the conduit and one below the crack at about 85 m down the conduit. The grey bars indicate locations where the fracture transfer function should explain the resultant resonant mode. The red bar indicates the coupled mode associated with top section of the conduit at about 1 Hz. Panel (c) shows the fracture transfer function for this crack.

middle of the conduit. This behavior can be seen when comparing Figures 10 and 12. In the space-time plots we can see an increase in the pressure amplitude being transmitted past the fracture at about 2.05 seconds in Figure 12 compared to Figure 10. We also see a decrease in the reflected pressure amplitude. In the frequency spectrum the higher order organ pipe modes associated with the upper conduit section decrease in amplitude with increasing dip, but the crack wave modes do not appear to change amplitude for the steeply dipping fracture for this case.

Multiple Crack Geometry

Finally we present results from a multi-crack system. Due to the linearity of our system, we would expect more complicated systems to exhibit a superposition of modes represented in simpler single crack geometries. We now consider a three crack system where the cracks are located at 50 m, 100 m and at the base of the conduit (150 m); and the cracks at 50 and 100 m have a length of 5m where the crack at 150 m has a length of 10 m. Additionally, the crack at 50 m has a width of 0.08 mm and the lower two cracks have widths of 80 mm. Figure 13 shows the resulting frequency spectra and space-time plot for this geometry. If we were to consider each of these cracks seperately we'd expect to see a mode of 0.2 Hz from the basal crack geometry, modes of 1.2 and 6 Hz from the thick middle crack, and modes of 4 and 8 Hz from the thin middle crack. Figure 13 shows that only the modes associated with the basal crack and the thick middle crack manifest. The opening to the thin crack is likely too small for enough energy to be transmitted into the fracture, and thus it does not resonate. In Figure 13, the red bar highlights the coupled mode for the 150 m conduit and the basal crack. The green bar highlights the coupled mode for the top 100 m conduit connected

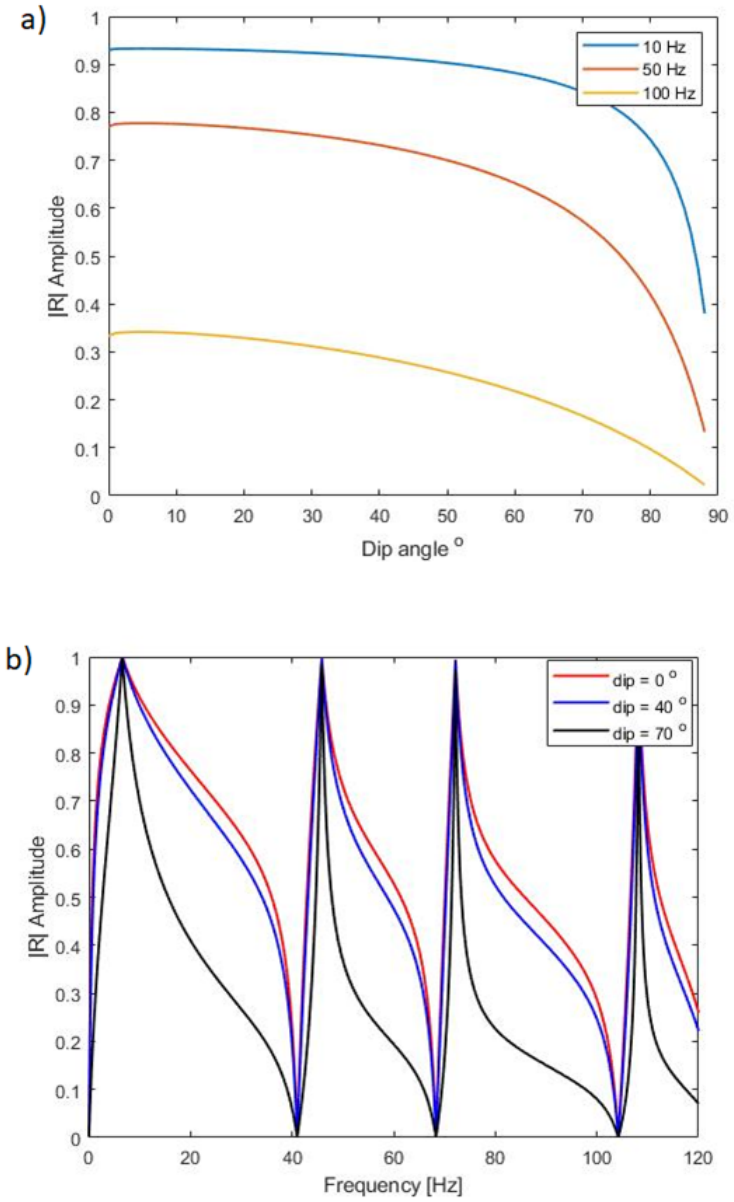

Figure 11. Effect of crack dip angle on the reflection coefficient. Panel (a) shows how the reflection coefficient varies with dip angle for multiple frequencies. Panel (b) Shows how the reflection coefficient varies with frequency for various dip angles.

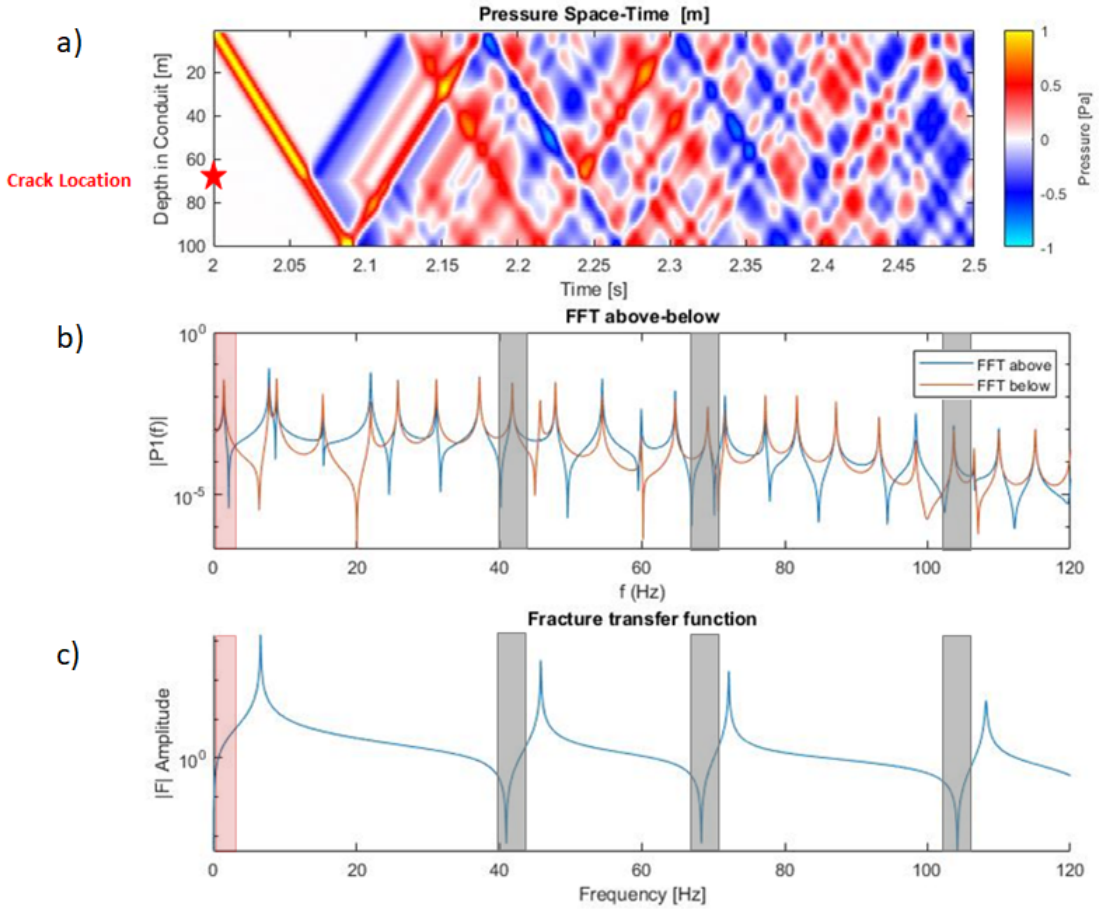

Figure 12. Similar to Figure 10, but with a crack dipping at 70 degrees. Panel (a) shows pressure changes through the conduit in time and the crack location is marked with a red star. Panel (b) shows the Fast Fourier Transform of two pressure time series, one above the crack at about 35 m down the conduit and one below the crack at about 85 m down the conduit. The grey bars indicate locations where the fracture transfer function should explain the resultant resonant mode. The red bar indicates the coupled mode associated with top section of the conduit at about 1 Hz. Panel (c) shows the fracture transfer function for this crack.

to the thick middle crack. And finally the mode at around 6 Hz is an organ pipe mode assocaited with the top 100 m conduit. While multi-crack systems were not rigorously explored in this study, this example shows the possibility of explaining complicated systems as a superposition of the modes seen in the simpler geometries. Finally we would like to note that it is likely that other coupled modes may arise for more complex geometries, but we leave this investigation to future work.

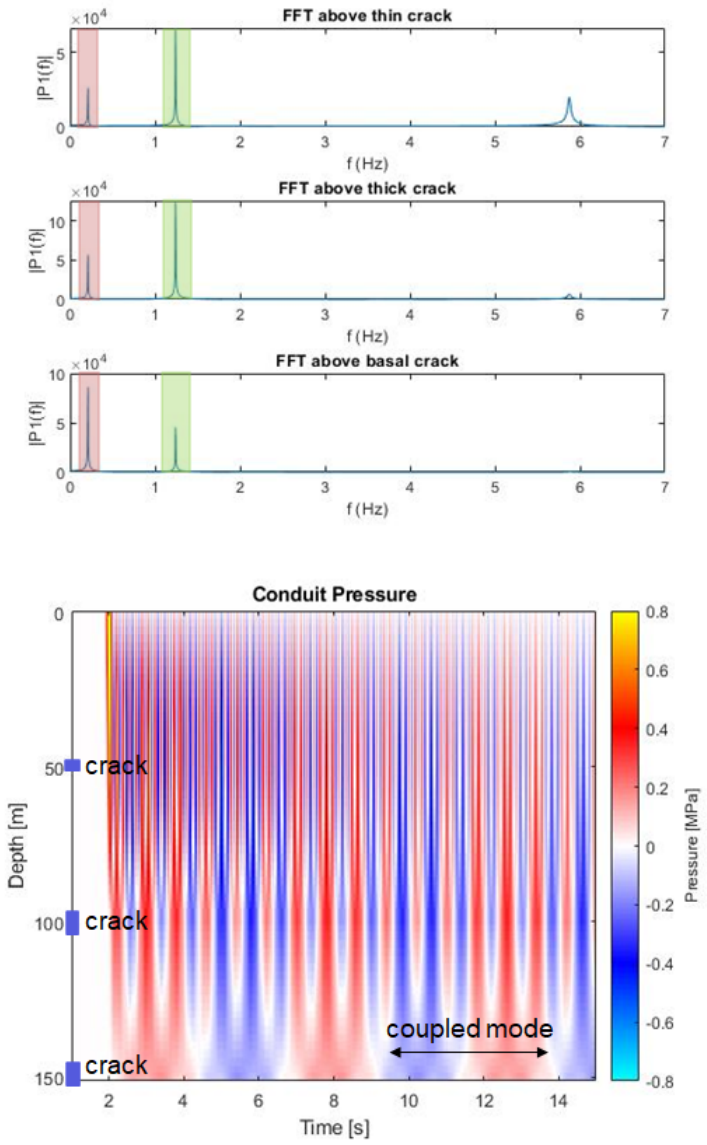

Figure 13. Here we show the results of a three crack system where the cracks are at 50 m, 100 m and 150 m down the conduit. The top two cracks have a length of 5 m and the basal crack has a length of 10 m. The top crack at 50 m has a very small width of 0.08 mm compared to 80 mm for the remaining two cracks. In the Fourier domain plot, the red bar denotes the coupled mode for the basal crack, and the green bar denotes the coupled mode for the crack at 100 m.

CHAPTER V

DISCUSSION

Fluid resonance has many promising applications in the englacial setting. In this section, we apply our results from the previous section to inform future experiments by providing metrics for determining englacial geometry based on fracture resonance and further discuss the limits of its usefulness to glaciologists.

Fracture Resonance

Previous studies have used two observables to predict crack geometry, the fundamental crack wave frequency from the fracture, and the quality factor for this mode. Where quality factor has to do with the attenuation rate of the signal and is defined as $Q = \frac{f}{\Delta f}$, where f is the fundamental frequancy and Δf is the full width at half-maximum (FWHM) of the fundamental frequency. Lipovsky and Dunham 2015 applied this method to a glacial parameter space and produced the red and black contour lines seen in Figure 14. The red contour lines are the fundamental frequency in Hz and the black lines are the quality factors. The thick black line represents where the quality factor is below $\frac{1}{2}$ and the system is considered overdamped meaning no resonance can occur. Additionally, the data points on this plot represent possible fracture geometries for frequencies recorded at the Kamb and MacAyeal ice streams as well as Bering Glacier (Anandakrishnan and Alley 1997, Winberry et al 2009, West et al 2010). The Kamb data point is outlined in red because the observed frequencies showed equally spaced resonant modes, indicating these modes were not dispersive and are likely not crack waves. In Lipovsky and Dunham's study, they assumed a fracture with only one length dimension. We expanded this to two length dimensions and show the resulting fundamental frequencies as the blue contours. For this study, we do not attempt

to revise their estimates of quality factor due to our assumption of Poiseuille flow. This assumption likely leads to an overestimation of viscous damping and thus an inaccurate quality factor. We leave a more detailed investigation into quality factors for future work. If we compare our results to the previous work of Lipovsky and Dunham, we see that neglecting one length dimension leads to over-estimating the fracture width and length.

Additionally, we consider the effects of asymmetry on the fracture fundamental mode. Figure 15 shows how the fundamental mode of the fracture varies for different fracture openings and a range of crack lengths. Here the x-axis is the log of the crack length in the x direction and the y-axis is the log of the crack length in the y-direction. The red and blue contours denote the fundamental crack frequency for different fracture widths. This figure shows that crack asymmetry results in non-unique fundamental frequencies for certain crack geometries. For example if we consider a crack length of 10 m in the x-direction. We see that the fundamental frequency could be anywhere between 30 and 0.4 Hz depending on the length in the y-direction. This non-uniqueness could potentially be an issue when trying to determine the geometry of real life fractures.

Detecting Branching Fractures From a Conduit

We now apply our knowledge of the coupled mode and crack waves modes to previously published results by Graff et al. 2019. They recorded resonant frequencies from a borehole connected to a basal crack on Rhonegletscher Glacier in the Swiss Alps and analyzed their results in the context of crack wave resonance described by Lipovsky and Dunham 2015. However, with our understanding of the coupled mode that can arise in this geometry, we interpret their results a bit differently. Graff et al. 2019 observed two high amplitude low frequency signals

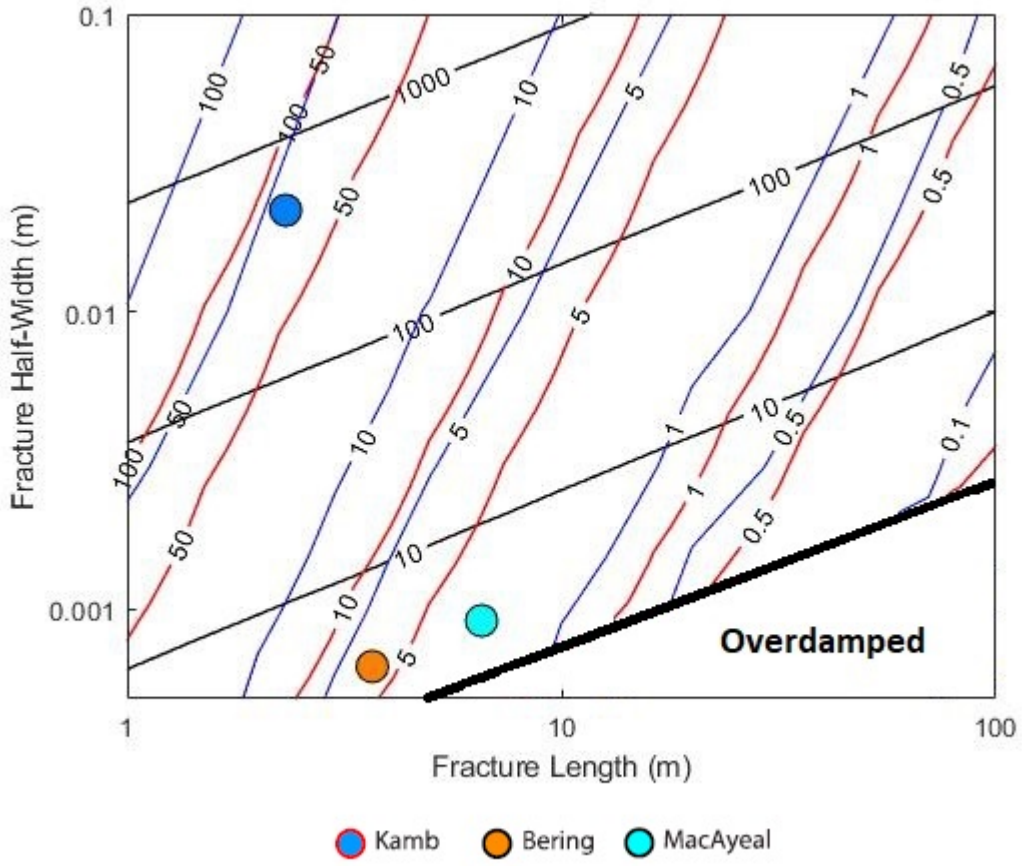

Figure 14. Plot to relate fracture fundamental frequency to crack length and half width for a 3D crack with two equal length dimensions. Red and blue contour lines represent the fundamental frequency of the fracture in Hz. Red contour lines are results from Lipovsky and Dunham 2015. They show fracture fundamental frequency for a 2D crack with one length dimension. Blue contour lines are the results from this study. Black contour lines represent the quality factor from Lipovsky and Dunham's analysis. The thick black contour represents where the quality factor is 1/2. Below this region all frequencies are considered over-damped. Data point locations were determined through Lipovsky and Dunham's analysis. Kamb ice stream is circled in red due to the fact that it exhibited equally spaced resonant modes, indicating a lack of crack waves.

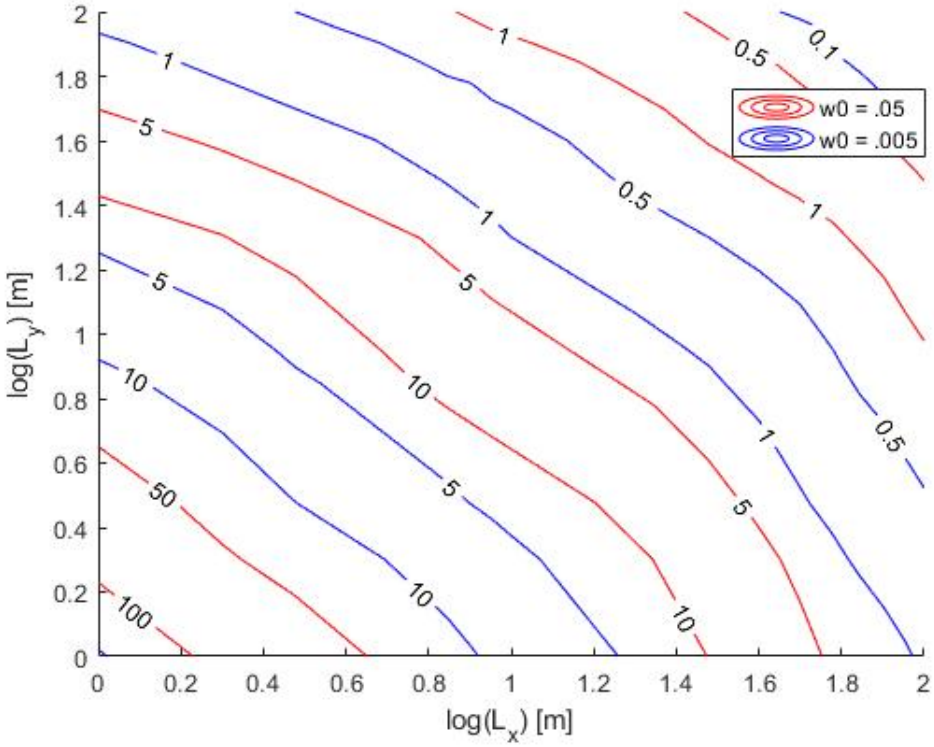

Figure 15. Contours in blue and red denote the fundamental crack wave mode for different fracture widths. We vary crack length on the x and y axes and show that the fundamental mode varies with asymmetry.

that are not related to possible organ pipe modes, and thus they interpret them as crack waves from the fracture. However, our study suggests that the fundamental mode should be the coupled mode we discussed earlier, we thus interpret the 1 Hz mode to be the coupled mode and the 4 Hz mode to be the fundamental mode of the fracture. Using equation (3.13) and a calculated kappa value of 0.56388, we calculate the fracture length to be about 4 m, much smaller than the predicted 19.8 m predicted from the interpretation from Graff et al. 2019. Next we use the frequency of 4 Hz as the fundamental mode of the fracture and turn to Figure 16 to predict fracture geometry using this method. For a fracture with a fundamental mode of 4 Hz and a quality factor of about 4 (Figure 4 of Graff et al. 2019 was used to determine the quality factor) gives us a fracture length of about 4 m and a width of 0.8 mm. Our interpretation provides two separate crack related resonant frequencies that predict much smaller crack lengths than previously predicted and a reasonable crack width for the basal water layer in ice.

Graff et al. 2019 provides important insight on resonant features in the alpine environment, but for larger ice sheets it may be possible to have kilometer long water filled conduits connected to very large fractures. Figure 8 shows how the coupled mode frequencies vary based on conduit length, conduit radius and crack length. Additionally, the red line in the bottom two plots indicate where $\gamma = 1$. These plots can help us understand when the coupled mode could be useful for determining crack geometry in ice sheets. The middle plot in Figure 8 puts constraints on the crack lengths that the coupled mode can detect. The red $\gamma = 1$ line indicates that after $Lx = 60$ m, cracks are no longer in the elastically dominant regime, however, frequencies in the transitional regime still have a dependence on crack length until the expected frequencies flatten out. This

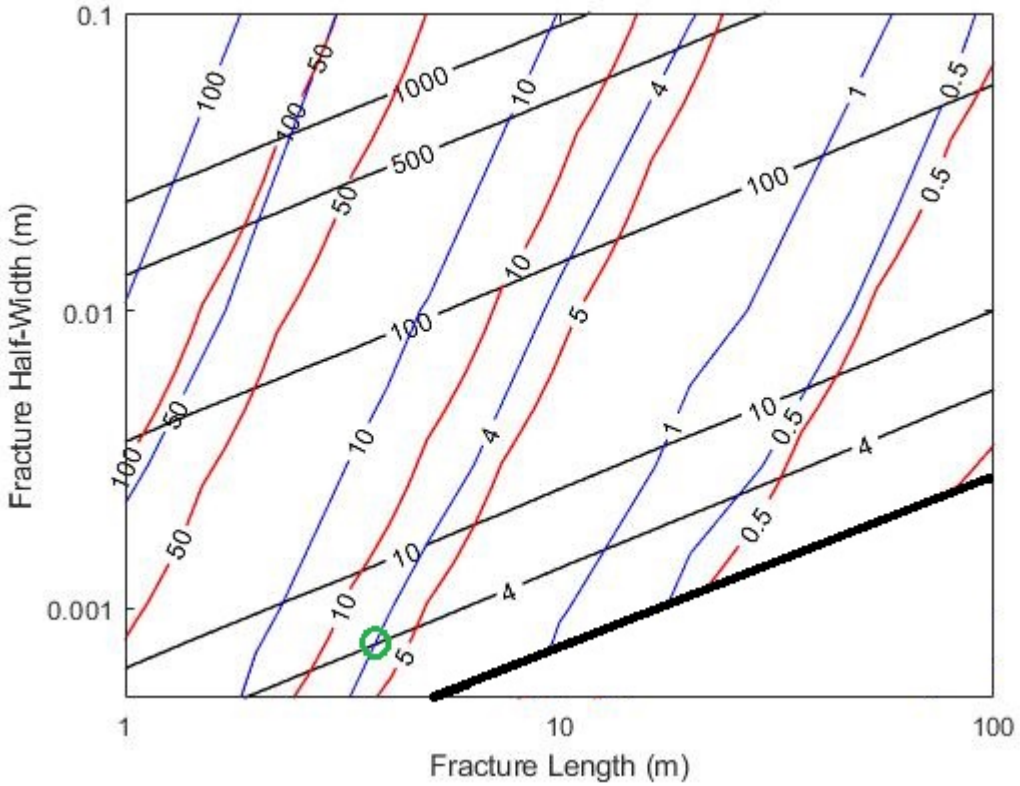

Figure 16. Similar to Figure 14, but we have included an additional frequency contour at 4 Hz and a quality factor contour at 4. The green circle highlights the intersection of these two contours and denotes the expected crack dimensions for our interpretation of the Graff et al. 2019 data.

suggests that crack geometry can still be determined for cracks up to 250 m. The bottom panel in Figure 8 suggests that conduit radii will likely need to increase with increasing crack length to remain in the elastic limit or transitional regime. It is possible that natural conduits connected to basal features will be moulins and might have radii even larger than our maximum radii shown in Figure 8, indicating this method could likely still be effective in this environment.

CHAPTER VI

CONCLUSION

Englacial geometry is an elusive missing piece for the glacial hydrologic system. We have investigated the extent to which fluid resonance in fractures and conduit-crack coupled systems can inform fracture length, width and conduit length. We present a number of tools that can be used to understand resonant behavior in simple conduit-crack geometries and we have applied these tools to a recent study to predict fracture length and width and produced plausible results for the englacial environment. We also suggest that this phenomenology can be scaled up for more complex systems with multiple fractures. In future work, we look forward to expanding our study on multiple fracture systems, investigating the effects of viscous dissipation for 3D fractures, and developing an experiment to further test this method in the field.

, , , ,, ,

REFERENCES CITED

Anandakrishnan, S., & Alley, R. B. (1997, July). Tidal forcing of basal seismicity of ice stream C, West Antarctica, observed far inland. *Journal of Geophysical Research: Solid Earth*, *102*(B7), 15183–15196. Retrieved 2020-07-09, from http://doi.wiley.com/10.1029/97JB01073 doi: 10.1029/97JB01073

Banwell, A., Hewitt, I., Willis, I., & Arnold, N. (2016, December). Moulin density controls drainage development beneath the Greenland ice sheet. *Journal of Geophysical Research: Earth Surface*, *121*(12), 2248–2269. Retrieved 2020-07-09, from https://onlinelibrary.wiley.com/doi/abs/10.1002/2015JF003801 doi: 10.1002/2015JF003801

Biot, M. A. (1952, September). Propagation of elastic waves in a cylindrical bore containing a fluid. *Journal of Applied Physics*, *23*(9), 997–1005. Retrieved 2020-07-09, from http://aip.scitation.org/doi/10.1063/1.1702365 doi: 10.1063/1.1702365

Carpenter, M. H., Gottlieb, D., & Abarbanel, S. (1994, April). Time-stable boundary conditions for finite-difference schemes solving hyperbolic systems: methodology and application to high-order compact schemes. *Journal of Computational Physics*, *111*(2), 220–236. Retrieved 2020-07-09, from https://linkinghub.elsevier.com/retrieve/pii/S0021999184710576 doi: 10.1006/jcph.1994.1057

Catania, G. A., Neumann, T. A., & Price, S. F. (2008). Characterizing englacial drainage in the ablation zone of the Greenland ice sheet. *Journal of Glaciology*, *54*(187), 567–578. Retrieved 2020-07-09, from https://www.cambridge.org/core/product/identifier/S002214300020868X/type/journal_article doi: 10.3189/002214308786570854

Del Rey Fernández, D. C., Hicken, J. E., & Zingg, D. W. (2014, May). Review of summation-by-parts operators with simultaneous approximation terms for the numerical solution of partial differential equations. *Computers & Fluids*, *95*, 171–196. Retrieved 2020-07-09, from https://linkinghub.elsevier.com/retrieve/pii/S0045793014000796 doi: 10.1016/j.compfluid.2014.02.016

Dunham, E. M., & Ogden, D. E. (2012, May). Guided waves along fluid-filled cracks in elastic solids and instability at high flow rates. *Journal of Applied Mechanics*, *79*(3), 031020. Retrieved 2020-07-09, from https://asmedigitalcollection.asme.org/appliedmechanics/article/doi/10.1115/1.4005961/456058/Guided-Waves-Along-FluidFilled-Cracks-in-Elastic doi: 10.1115/1.4005961

Erickson, B. A., O'Reilly, O., & Nordström, J. (2019, December). Accuracy of stable, high-order finite difference methods for hyperbolic systems with non-smooth wave speeds. *Journal of Scientific Computing*, *81*(3), 2356–2387. Retrieved 2020-07-09, from http://link.springer.com/10.1007/s10915-019-01088-w doi: 10.1007/s10915-019-01088-w

Fountain, A. G., Schlichting, R. B., Jansson, P., & Jacobel, R. W. (2005). Observations of englacial water passages:a fracture-dominated system. *Annals of Glaciology*, *40*, 25–30. Retrieved 2020-07-09, from https://www.cambridge.org/core/product/identifier/S0260305500255328/type/journal_article doi: 10.3189/172756405781813762

Gräff, D., Walter, F., & Lipovsky, B. P. (2019, September). Crack wave resonances within the basal water layer. *Annals of Glaciology*, *60*(79), 158–166. Retrieved 2020-07-09, from https://www.cambridge.org/core/product/identifier/S0260305519000089/type/journal_article doi: 10.1017/aog.2019.8

Holzhausen, G., & Egan, H. (1986). Fracture diagnostics in east texas and western colorado using the hydraulic-impedance method. In *SPE Unconventional Gas Technology Symposium.* Louisville, Kentucky: Society of Petroleum Engineers. Retrieved 2020-07-09, from http://www.onepetro.org/doi/10.2118/15215-MS doi: 10.2118/15215-MS

Karlstrom, L., & Dunham, E. M. (2016, June). Excitation and resonance of acoustic-gravity waves in a column of stratified, bubbly magma. *Journal of Fluid Mechanics*, *797*, 431–470. Retrieved 2020-07-09, from https://www.cambridge.org/core/product/identifier/S0022112016002573/type/journal_article doi: 10.1017/jfm.2016.257

Liang, C., Karlstrom, L., & Dunham, E. M. (2020, January). Magma oscillations in a conduit-reservoir system, application to very long period (Vlp) seismicity at basaltic volcanoes: 1. Theory. *Journal of Geophysical Research: Solid Earth*, *125*(1). Retrieved 2020-07-09, from https://onlinelibrary.wiley.com/doi/abs/10.1029/2019JB017437 doi: 10.1029/2019JB017437

Liang, C., O'Reilly, O., Dunham, E. M., & Moos, D. (2017, May). Hydraulic fracture diagnostics from Krauklis-wave resonance and tube-wave reflections. *GEOPHYSICS*, *82*(3), D171–D186. Retrieved 2020-07-09, from http://library.seg.org/doi/10.1190/geo2016-0480.1 doi: 10.1190/geo2016-0480.1

Lighthill, J. (n.d.). *Waves in Fluids*. Cambridge University Press, 2001.

Lipovsky, B. P., & Dunham, E. M. (2015, February). Vibrational modes of hydraulic fractures: Inference of fracture geometry from resonant frequencies and attenuation. *Journal of Geophysical Research: Solid Earth*, *120*(2), 1080–1107. Retrieved 2020-07-09, from https://onlinelibrary.wiley.com/doi/abs/10.1002/2014JB011286 doi: 10.1002/2014JB011286

Molenaar, M. M., Hill, D., Webster, P., Fidan, E., & Birch, B. (2012, March). First downhole application of distributed acoustic sensing for hydraulic-fracturing monitoring and diagnostics. *SPE Drilling & Completion*, *27*(01), 32–38. Retrieved 2020-07-09, from http://www.onepetro.org/doi/10.2118/140561-PA doi: 10.2118/140561-PA

Mondal, S. (2010). *Pressure transients in wellbores: Water hammer effects andimplications for fracture diagnostics* (Unpublished doctoral dissertation). The University of Texas at Austin.

O'Reilly, O., Dunham, E. M., & Nordström, J. (2017, January). Simulation of wave propagation along fluid-filled cracks using high-order summation-by-parts operators and implicit-explicit time stepping. *SIAM Journal on Scientific Computing*, *39*(4), B675–B702. Retrieved 2020-07-09, from https://epubs.siam.org/doi/10.1137/16M1097511 doi: 10.1137/16M1097511

Podolskiy, E. A. (2020, March). Toward the acoustic detection of two-phase flow patterns and helmholtz resonators in englacial drainage systems. *Geophysical Research Letters*, *47*(6). Retrieved 2020-07-09, from https://onlinelibrary.wiley.com/doi/abs/10.1029/2020GL086951 doi: 10.1029/2020GL086951

Roeoesli, C., Walter, F., Ampuero, J.-P., & Kissling, E. (2016, August). Seismic moulin tremor: seismic moulin tremor. *Journal of Geophysical Research: Solid Earth*, *121*(8), 5838–5858. Retrieved 2020-07-09, from http://doi.wiley.com/10.1002/2015JB012786 doi: 10.1002/2015JB012786

Rona, A. (2007, October). The acoustic resonance of rectangular and cylindrical cavities. *Journal of Algorithms & Computational Technology*, *1*(3), 329–356. Retrieved 2020-07-09, from http://journals.sagepub.com/doi/10.1260/174830107782424110 doi: 10.1260/174830107782424110

Schoof, C. (2010, December). Ice-sheet acceleration driven by melt supply variability. *Nature*, *468*(7325), 803–806. Retrieved 2020-07-09, from http://www.nature.com/articles/nature09618 doi: 10.1038/nature09618

Sheriff, R. E., & Geldart, L. P. (1995). *Exploration seismology* (2nd ed ed.). Cambridge ; New York: Cambridge University Press.

Vatne, G. (2001, June). Geometry of englacial water conduits, Austre Brøggerbreen, Svalbard. *Norsk Geografisk Tidsskrift*, *55*(2), 85–93. Retrieved 2020-07-09, from http://www.catchword.com/cgi-bin/cgi?body=linker&ini=xref&reqdoi=10.1080/00291950152105136 doi: 10.1080/00291950152105136

West, M. E., Larsen, C. F., Truffer, M., O'Neel, S., & LeBlanc, L. (2010, April). Glacier microseismicity. *Geology*, *38*(4), 319–322. Retrieved 2020-07-09, from http://pubs.geoscienceworld.org/geology/article/38/4/319/130206/Glacier-microseismicity doi: 10.1130/G30606.1

Winberry, J. P., Anandakrishnan, S., & Alley, R. B. (2009, June). Seismic observations of transient subglacial water-flow beneath MacAyeal Ice Stream, West Antarctica. *Geophysical Research Letters*, *36*(11), L11502. Retrieved 2020-07-09, from http://doi.wiley.com/10.1029/2009GL037730 doi: 10.1029/2009GL037730

Womersley, J. R. (1955, March). Method for the calculation of velocity, rate of flow and viscous drag in arteries when the pressure gradient is known. *The Journal of Physiology*, *127*(3), 553–563. Retrieved 2020-07-09, from http://doi.wiley.com/10.1113/jphysiol.1955.sp005276 doi: 10.1113/jphysiol.1955.sp005276